



**Stretchable Solid-State Zinc Ion Battery Based on Cellulose
Nanofiber-Polyacrylamide Hydrogel Electrolyte and
Mg_{0.23}V₂O₅·1.0H₂O Cathode**

Journal:	<i>Journal of Materials Chemistry A</i>
Manuscript ID	TA-ART-07-2020-006467.R1
Article Type:	Paper
Date Submitted by the Author:	30-Jul-2020
Complete List of Authors:	Xu, Wangwang; Louisiana State University, Mechanical Engineering Liu, Chaozheng; Nanjing Forestry University, Wu, Qinglin; Louisiana State University System, ; Xie, Weiwei; Louisiana State University, Chemistry Kim, Won-Yeong ; UNIST Lee, Sang-Young; UNIST, Interdisciplinary School of Green Energy Gwon, Jae-Gyoung; Korea Forest Research Institute, Forest Products

ARTICLE

Stretchable Solid-State Zinc Ion Battery Based on Cellulose Nanofiber-Polyacrylamide Hydrogel Electrolyte and $\text{Mg}_{0.23}\text{V}_2\text{O}_5 \cdot 1.0\text{H}_2\text{O}$ Cathode

Received 00th January 20xx,
Accepted 00th January 20xx

DOI: 10.1039/x0xx00000x

Wangwang Xu^a, Chaozheng Liu^b, Qinglin Wu^{a, *}, Weiwei Xie^c, Won-Young Kim^d, Sang-Young Lee^d and Jaegyong Gwon^e

In comparison with well-protected rigid batteries with liquid electrolytes, solid-state battery (ssB) is more beneficial to offer high flexibility, high wearability and leakage prevention. Currently, ssB with the capability of bending and twisting has been extensively studied. However, it remains a challenge to develop to a highly stretchable ssB with the maintenance of high performance. Herein, we report a stable solid-state zinc ion battery (ssZIB) based on cellulose nanofiber (CNF)-polyacrylamide (PAM) hydrogel electrolyte and $\text{Mg}_{0.23}\text{V}_2\text{O}_5 \cdot 1.0\text{H}_2\text{O}$ cathode. The designed CNF-PAM hydrogel shows a high stretchability and robust mechanical stability. Moreover, the porous CNF-PAM hydrogel electrolyte provides efficient pathways for the transportation for zinc ions. And the robust layered structure of $\text{V}_2\text{O}_5 \cdot 1.0\text{H}_2\text{O}$ pillared with Mg^{2+} ions and water support the fast insertion/extraction of zinc ions in lattice. Therefore, the designed ssZIB shows unprecedented high capacity at high current with durable cycling life. At the current density of 5 A/g (charging time of around 3 minute), the ssZIBs can deliver high reversible capacity of 216 mAh/g after 2000 cycles, and retain 98.6% of the initial capacity, showing a high capacity and long-life durability at high currents. Furthermore, the designed spring ssZIBs are workable under stretching with the strain reaching 650%. And the designed ssZIBs are still operational even under repeated bending, freezing, and heating conditions. The ssZIBs show robust mechanical stability, high stretchability and impressive electrochemical performance, providing a potential pathway to expand the application of ZIBs to broad practical energy storage devices.

1. Introduction

The development of flexible and wearable electronic devices has triggered extensive research on batteries with special features such as flexibility, safety and high performance.^{1, 2, 3} In comparison with well-protected rigid batteries with liquid electrolytes, solid-state batteries (ssBs) are more beneficial to offer high flexibility, high wearability and leakage prevention.⁴⁻⁶ In the past several decades, lithium ion batteries (LIBs) have dominated the market of energy storage devices due to their high energy density.^{7, 8, 9} However, it is still very challenging to expand their application to a larger field, especially flexible energy storage devices.^{10, 11} Most of reported flexible LIBs show a series of hidden safety issues such as explosion and fire due to the flammable and toxic electrolytes.¹² The flexible

aqueous LIBs also suffer from poor cyclic stability and low energy density.^{13, 14} In recent years, novel zinc ion batteries (ZIBs) are emerging as the promising energy storage devices to substitute LIBs for large-scale applications due to low cost, abundant resources, and environmental friendliness.^{[3], 15-18} The rechargeable ZIBs are able to perform with low-flammability and high-safety hydrogel electrolyte due to the low redox potential of Zn^{2+}/Zn (-0.76 V).^{19, 20} In addition, the high flexibility of hierarchical polymer electrolyte can give the wearability and superior shear resistance for ssZIBs.²¹

ssZIBs are composed of four components including cathode, anode (zinc metal), solid electrolyte and current collectors.^{22, 23} The gel electrolyte is sandwiched between the cathode and anode. Each component has a significant effect on the performance of the whole battery. Currently, various gel electrolytes have been studied and have been applied in ZIBs.^{24, 25-29} However, the performance of ssZIBs are still not comparable with the batteries using liquid electrolyte, especially high rate capability, due to the low ionic conductivities of the gel electrolytes. To realize high ionic conductivity, ideal gel electrolyte requires a high-water content, efficient ion migration channels, combined with reasonable mechanical property. As one of the most principal natural polymers, cellulose nanofibers (CNFs) are widely used as a sustainable reinforcing additive in various composites.^{30, 31} In addition, the hydrophilic skeleton of CNFs and their three-dimensional fiber network with large space can help stabilize the channels for chargers transportation.²² Furthermore, due to the abundant hydroxyl groups on the surface of CNFs, it is

a. School of Renewable Natural Resources, Louisiana State University AgCenter, Baton Rouge, Louisiana 70803, United States, E-mail: qwu@agcenter.lsu.edu (Q. Wu). Phone: 225-578-8369. Fax: 225-578-4251.

b. College of Materials Science and Engineering, Nanjing Forestry University, Nanjing, China.

c. Department of Chemistry, Louisiana State University, Baton Rouge, Louisiana 70803, United States.

d. Department of Energy Engineering, School of Energy and Chemical Engineering, Ulsan National Institute of Science and Technology (UNIST), Ulsan 689-798, South Korea.

e. Forest products department, National institute of Forest Science, 57 Hoegiro, Dongdaemun-gu, Seoul 02455, South Korea.

facile to link the CNFs with polyacrylamide (PAM) molecular chains through hydrogen bonding.^{21, 32} The combination of CNF and PAM can serve as effective solid electrolyte with high mechanical properties and high ionic conductivity. Due to the high thermal stability of hydrogel polymers, ssBs are also able to operate at both low and high temperature condition, which is critical for the applications of batteries at some harsh environments such as cold/frozen regions, and flying airplanes in space.^{22, 25}

Ideal hydrogel electrolyte alone is not enough to realize high rate performance for ssZIBs. Cathode material is also crucial. Even though the ionic radius of Zn^{2+} ions is small, the diffusion of Zn^{2+} ions in cathode materials is sluggish due to the large solvation sheath and high charge of Zn^{2+} ions.^{33, 34} In recent years, tremendous research effort has been devoted in designing advanced cathode materials for ultrafast ZIBs. For example, to design a superfast cathode, Yang *et al.* synthesized vanadium dioxide (VO_2 (B)) nanofibers for Zn^{2+} ions insertion and extraction.³⁵ With unique and big tunnel structure, VO_2 (B) nanofibers can accommodate super-fast intercalation of zinc ions with little structure change. Therefore, VO_2 (B) nanofibers show excellent rate capability. At current of 51.2 A/g, VO_2 (B) nanofibers deliver the specific capacity of 171 mAh/g. However, compared with layered V_2O_5 , VO_2 (B) shows lower theoretical capacity and fewer ion diffusion pathways. Synthesizing V_2O_5 with chemically preintercalated ions is an effective way to enhance the rate capability due to the larger interlayer spacing and stable pillared layered structure. For example, Liang *et al.* designed Li^+ ion intercalated $\text{V}_2\text{O}_5 \cdot n\text{H}_2\text{O}$ as cathode for ZIBs.³⁶ The $\text{Li}_x\text{V}_2\text{O}_5 \cdot n\text{H}_2\text{O}$ shows high rate performance and long cycling life. At current of 10 A/g, $\text{Li}_x\text{V}_2\text{O}_5 \cdot n\text{H}_2\text{O}$ supported specific capacity of 192 mAh/g for 1000 cycles. The remarkable performance attributes to the enlarged layer spacing to facilitate the fast diffusion of Zn^{2+} ions. Compared with the radius of hydrated lithium ions (0.38 nm), the radius of hydrated magnesium ions is much larger (0.43 nm). V_2O_5 pillared with magnesium ions can maintain the bilayer crystal structure and show larger interlayer spacing. Moreover, compared with most metal elements (K, Fe, Ca, and Al e. g.), the molar mass of Mg is smaller.³⁷ Therefore, it is expected that the V_2O_5 pillared with Mg^{2+} can possess higher theoretical capacity and rate capability.

Herein, we report a superfast and stable ssZIB based on CNF-PAM hydrogel electrolyte and $\text{Mg}_{0.23}\text{V}_2\text{O}_5 \cdot 1.0\text{H}_2\text{O}$ (MVO) cathode. The hydrogel electrolyte was prepared using natural CNFs combined with PAM *via* a free radical polymerization of acrylamide monomers. And the MVO cathode was synthesized *via* a facile hydrothermal method. The designed ssZIBs show unprecedented high capacity at high currents with durable cycling life. At the current density of 5 A/g, the ssZIBs can provide the reversible capacity of 216 mAh/g within charging time of only 3 minutes for over 2000 cycles, showing a high capacity and long-life durability. Moreover, at the extremely high current density of 20 A/g (charging time of around 12 seconds), the ssZIBs can deliver the reversible specific capacity of about 62 mAh/g after 20000 cycles, showing long-life stability at high rates. This excellent electrochemical performance attributes to both CNF-PAM hydrogel electrolyte and the novel MVO microspheres cathode. The porous CNF-PAM hydrogel electrolyte provides efficient pathways for the transportation for zinc ions. In addition, the robust layered structure of MVO microspheres supports the fast insertion/extraction of zinc ions in lattice. *Ex-site* XRD, Raman spectrum, XPS and TEM

techniques were used to systemically study the electrochemical reaction mechanism of the material and the structure change with the accommodation of zinc ions. More importantly, the designed CNF-PAM hydrogel shows a high stretchability (730%) and high strength (200 kPa), which enables the robust mechanical performance of the designed ssZIBs. For demonstration, a spring-type ssZIB was made to power a digital clock, which was still workable under repeated stretching.

2. Experimental section

2.1 Preparation of polymer electrolyte for ssZIBs

To assemble the ssZIBs, the polymer electrolyte was synthesized *via* polymerization of PAM combined with CNFs. Specifically, 1.33 g CNFs (1.5 wt % water suspension, University of Maine, Orono, ME, USA) were first dispersed in 20 ml 1 M $\text{Zn}(\text{CF}_3\text{SO}_3)_2$ solution with extensive high-speed stirring.³⁸ After that, 50 mg ammonium persulfate, 3 g acrylamide (AM) monomers and 50 mg N, N'-methylenebisacrylamide (BIS) were added to the suspension. After being stirred at 25 °C for 2 h, the mixture was cast onto a glass petri dish. Then, the formed membrane was put in an oven and heated at 60 °C for half an hour. During this heating treatment, acrylamide was grafted onto the CNF surface through free radical polymerization. Finally, after being cooled to room temperature, the crosslinked CNF-PAM film was obtained. The prepared polymeric film shows high flexibility, applicable as solid-state separator directly.

2.2 Synthesis of MVO microspheres

In a typical process,³⁷ 1.09 g V_2O_5 was dispersed in 48 mL deionized water and the mixture was stirred for 5 minutes. Then, 12 mL hydrogen peroxide (30%) was dropwise added into the suspension. After stirring for one hour, a transparent red suspension was obtained. After that, 0.528 g $\text{Mg}(\text{NO}_3)_2$ was dissolved in a separated 10 mL deionized water. Next, the $\text{Mg}(\text{NO}_3)_2$ suspension was dropwise added into the above solution under continuous stirring. The mixture was then transferred into a Teflon-lined autoclave and heated at 200 °C for 48 h. After the autoclave was cooled to room temperature, red-color precipitates were collected by centrifuging and washed with deionized water and alcohol for several times separately. After being dried at 60 °C for overnight, the MVO microsphere sample was obtained.

2.3 Preparation of spring ssZIBs

The spring battery was designed *via* using a polyurethane spring tube. The cathode electrodes were first prepared by coating a homogeneous slurry of 80 wt.% MVO, 20 wt.% carbon black, 10 wt.% polyvinylidene fluoride (PVDF) in 1-methyl-3-pyrrolidone (NMP) solvent on a narrow stainless-steel film and then dried in oven at 60 °C for 12 h. Zinc metal wire was used as anode. After the cathode and anode electrodes inserted into the spring tube, the spring tube was filled with the mixed solution of electrolyte (1.33 g CNFs, 3 g acrylamide, 50 mg ammonium persulfate and 50 mg BIS in 20 ml 1 M $\text{Zn}(\text{CF}_3\text{SO}_3)_2$ solution). Then, the spring tube was put in an oven and heated at 60 °C for half an hour. During this heating treatment, the electrolyte was solidified due to the polymerization of acrylamide and crosslinking of PAM and CNFs. After being cooled to room temperature, the spring ssZIBs were obtained.

2.4 Characterization

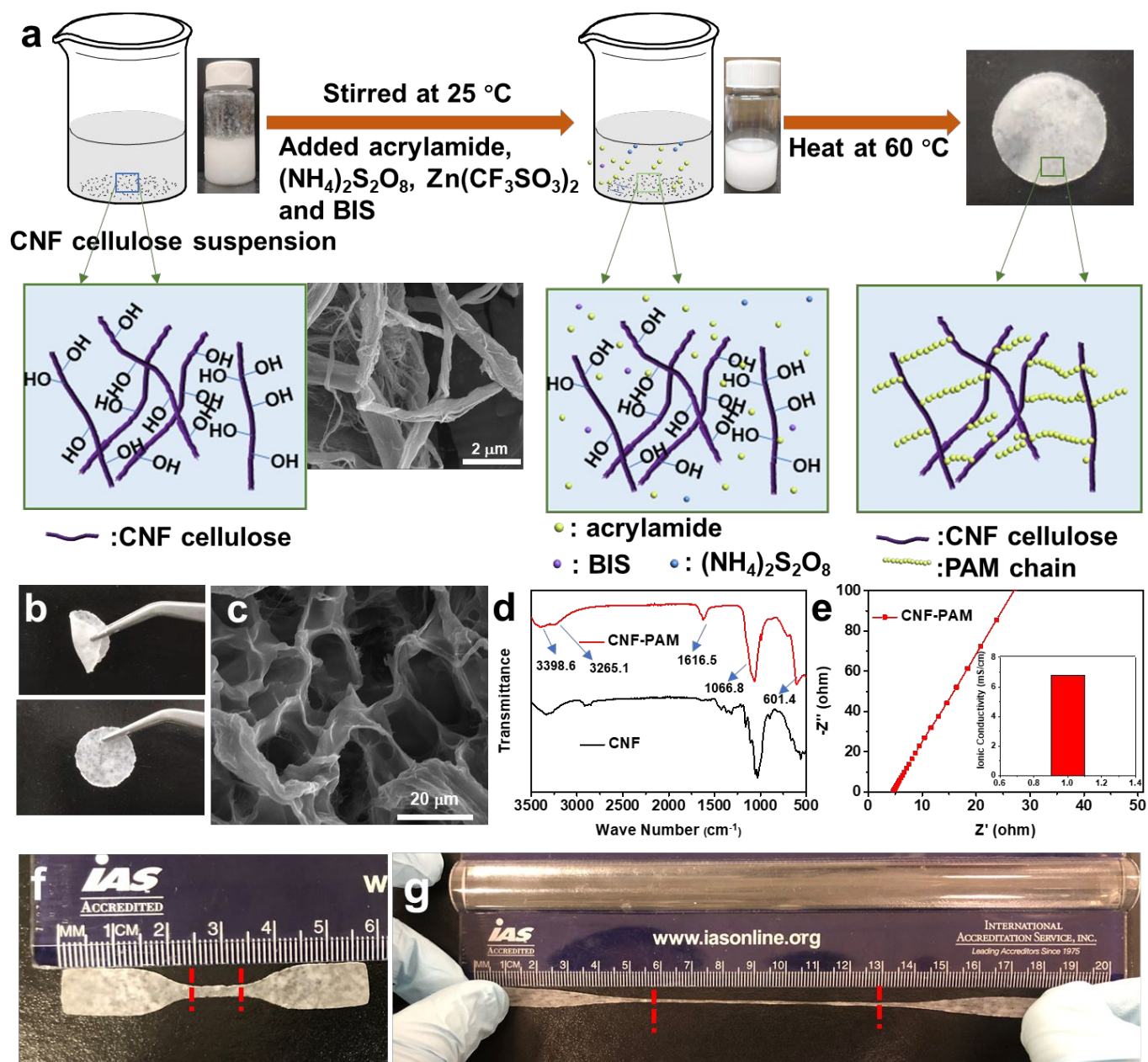


Figure 1. (a) Schematic of the synthesis route to form solid-state electrolyte by grafting PAM on CNFs *via* a facile free radical polymerization approach; (b) optical photos, (c) SEM image, (d) FTIR spectra of the obtained CNF-PAM film, (e) AC impedance of the CNF-PAM films with frequency range from 10 KHz to 0.01 Hz. Optical photos of (f) initial length and (g) stretched length (>700% stretching) of the prepared CNF-PAM film.

The x-ray diffraction (XRD) patterns of the samples were measured by a Rigaku MiniFlex XRD instrument (RIGAKU, Austin, TX, USA) with Cu K α radiation ($\lambda = 1.5405 \text{ \AA}$) from 10° to 90° 2θ range at a scan rate of $1^\circ/\text{min}$. Thermogravimetric analysis (TGA) was conducted using a Q50 analyzer (TA Instruments Inc, New Castle, DE, USA) with the heating rate of $1^\circ/\text{min}$ from 20°C to 600°C in nitrogen gas. Fourier Transform Infrared (FTIR) spectroscopy was carried out on a Thermo Scientific Nicolet 6700 (Waltham, Boston, MA, USA) spectrometer. The chemical states of all the products were studied by X-ray photoelectron spectroscopy (XPS) on an AXIS165 spectrometer (MRFN, Manchester, UK). Energy dispersive spectroscopic (EDS)

mapping and sample morphology were performed by a FEI Quanta 3D FEG field emission scanning electron microscopes (SEM) (FEI, Boston, MA, USA). High resolution transmission electron microscopy (HRTEM) images and selected area diffraction patterns (SAED) were conducted in a JEM-1400 (JEOL USA Inc., Peabody, MA, USA). Mechanical property of the gel electrolyte film was tested in tension with a model 5900R Instron machine (Instron Inc., Norwood, MA, USA).

2.5 Electrochemical Measurements

The electrochemical data was collected using assembled 2032-coin cells. The cathode electrode was prepared by mixing as-prepared

MVO microspheres or $V_2O_5 \cdot nH_2O$, carbon black and polytetrafluoroethylene (PTFE) binder at a weight ratio of 6:3:1. The coin cells were assembled using the prepared cathode, zinc metal as the anode, and the prepared PAM-CNF film as electrolyte and separator. Galvanostatic charge/discharge electrochemical test were performed on an eight-channel LAND battery analyzer (CT3001A, LAND Electronics Corporation, Wuhan, China) with the voltage range of 0.2 - 1.6 V. Cyclic voltammetry (CV) measurements were carried out on an electrochemical workstation (CHI 760e) with the potential range of 0.2-1.6 V. Electrochemical impedance spectroscopy (EIS) data were carried out by applying an AC potential of 5 mV amplitude with the frequency range of 0.01-100 kHz. Freeze-resistance test was carried out at -18 °C in a freezer. Heat-resistance properties were tested in EQ-DHG-9015 oven (MTI Inc, Richmond, CA, USA).

3. Results and Discussion

3.1 Fabrication of CNF-PAM Hydrogel Electrolyte

Fig. 1 displays the synthesis route of the CNF-PAM hydrogel electrolyte. During the heating process, acrylamide monomers were polymerized *via* free radical polymerization and grafted onto the CNFs by connecting with the numerous hydroxide and carboxyl bonds on the surface of CNFs. Optical photos in Fig. 1b and S1 reveal that the white, flexible, and all-solid-state CNF-PAM electrolyte was obtained. The thickness of CNF-PAM electrolyte was around 753.17 μm (Fig. S2). Fig. 1c and S3, S4 display the SEM and TEM micrographs of pure CNFs, pure PAM film and CNF-PAM electrolyte film. As shown in Fig. S3, the CNF itself can form a three-dimensional network morphology with large space, promoted by the long length of the fibers (5-200 nm). And the freeze-dried PAM film shows uniform micropores with the diameter ranging from 5-10 nm (Fig. S4a, b). While the PAM-CNF film shows much larger pores with the diameter of 5-30 nm. Compared with more individualized fibers of CNFs and clean PAM film, the CNF-PAM film shows a honeycomb-like morphology (Fig. S4c, d). In the PAM-CNF film, the CNF network serves as stable three-dimensional framework and PAM is anchored on the surface of CNF fibers, forming an integrated porous film. The pores are available for the filling of electrolyte, supporting efficient transportation pathways for charge carriers. As shown in Fig. 1d, the FTIR spectrum of the CNFs displays absorbance band at 3329.8, 2928.1, 1420.1 and 1045.2 cm^{-1} , which can be assigned to the bonds of O-H stretching vibration, C-H stretching, CH_2 bending, C-O bond of aliphatic C-OH vibration respectively. The FTIR spectra of the CNF-PAM film shows more absorption bands at 3265.1, 1616.5 cm^{-1} , which are attributed to the mode of N-H stretching vibration and C=O stretching vibration from PAM composition, indicating that CNF and PAM were both present in the prepared CNF-PAM electrolyte. In addition, as shown by the tensile sample picture and stress-strain curve in Fig. S5, the strength of CNF-PAM hydrogel film can reach 192 kPa, with a large strain of about 730%. As displayed in Fig. 1f and g, the CNF-PAM electrolyte film can be easily stretched to reach the strain rate of over 700% without apparent breakage, showing remarkable elastic property. The high strength and strain are attributed to the confinement of the network of CNFs and

polyacrylamide chains. Moreover, due to the large and stale pores available, the synthesized CNF-PAM gel electrolyte could absorb water over 100% of its own weight, with a high-water content of 61.55 wt%. Therefore, the high ionic conductivities of CNF-PAM gel electrolyte can be achieved. It is impressive that the CNF-PAM electrolyte exhibits a high ionic conductivity of 6.8 mS/cm . The high ionic conductivity of CNF-PAM electrolyte supports the high rate capability of MVO/Zn solid-state battery (SSB).

3.2 Formation Mechanism and Characterization of MVO Microspheres

The bilayer structured MVO microspheres were synthesized *via* a hydrothermal method. During the first step of the formation of V_2O_5 sol, V_2O_5 was partially reduced by H_2O_2 , leading to the phase transformation from VO_5 square pyramids to VO_6 octahedra. As a result, the bilayer structured V_2O_5 was formed with a large number of water molecules embedded into the interlayer space. The large interlayer space provided many pathways for the diffusion of the subsequent inserted Mg^{2+} ions. The intercalated Mg^{2+} ions resulted in the slippage and shrinkage of the layers due to the formation of magnesium oxygen octahedra. The coordination of magnesium and oxygen served as pillars between layers, supporting high stability of the lattice. Finally, the bilayer structured MVO was formed with thermodynamic driving.

As shown in Fig. 2a, the XRD pattern of $\text{Mg}_{0.23}\text{V}_2\text{O}_5 \cdot 1.0\text{H}_2\text{O}$ microspheres shows sharp diffraction peaks and is dominated along the pronounced (001) direction, indicating high preferred orientation along *c*-axis. Moreover, the (001) peak located at 6.42° indicates the wide interlayer spacing of 13.88 Å, showing much broadened interlayer spacing than that of $V_2O_5 \cdot n\text{H}_2O$ (Fig. S6). Similar XRD results are also observed in $\delta\text{-V}_2\text{O}_5$ with other preintercalated cations, such as CaV_2O_5 ,³⁹ $\text{Zn}_{0.25}\text{V}_2\text{O}_5$,⁴⁰ and $\text{Mg}_{0.3}\text{V}_2\text{O}_5 \cdot 1.1\text{H}_2\text{O}$.³⁷ We further calculated the structural parameter to be $a = 13.111$, $b = 6.1634$, and $c = 4.48$; $\alpha = 90^\circ$, $\beta = 92^\circ$, and $\gamma = 90^\circ$. As the structure shown in Fig. 2b and S7, the MgO_6 octahedra and water molecules act as pillars between the double-sheet V_2O_5 layers, similar to the σ -phase $\text{Zn}_{0.25}\text{V}_2\text{O}_5 \cdot n\text{H}_2\text{O}$ platelets.^{41, 42} The MgO_6 octahedra pin the V_2O_5 layers in *a-b* plane, which can accommodate the fast Zn^{2+} insertion, thus leading to high rate capability. Raman and FTIR spectrum further confirm the structure of $\text{Mg}_{0.23}\text{V}_2\text{O}_5 \cdot 1.0\text{H}_2\text{O}$ microspheres. The Raman spectrum (Fig. 2c) shows bands at 139.4, 192.5, 281.6, 404.7, 525.0, 691.4, and 990.8 cm^{-1} , which are the clear signature of layered vanadium pentoxide.^{43, 44} As the crystal structure shown in Fig. 2d, the Raman peaks at 990.8 and 691.4 cm^{-1} are assigned to the stretching vibration of the V-O_1 (terminal oxygen) and V-O_2 (doubly coordinated oxygen) bonds, respectively. The peak at 526 cm^{-1} corresponds to the V-O_2 (triply coordinated oxygen) stretching mode. The peaks located at 404.7 and 281.6 cm^{-1} are owing to the displacements of O_1 atoms along *X* and *Y* directions. The peak at 195 cm^{-1} corresponds to oscillating along the *x* axis. And the dominate peak at 139.4 cm^{-1} involves the shear motion and rotations of the ladders. The high intensity of this peak indicates the long-range order of the vanadium oxygen layers along the plane. The bending vibration mode of skeleton at 139.4 cm^{-1} and the stretching mode of V-O_1 at 990.8 cm^{-1} are the characteristic peaks of perfect layer-type structure of

ARTICLE

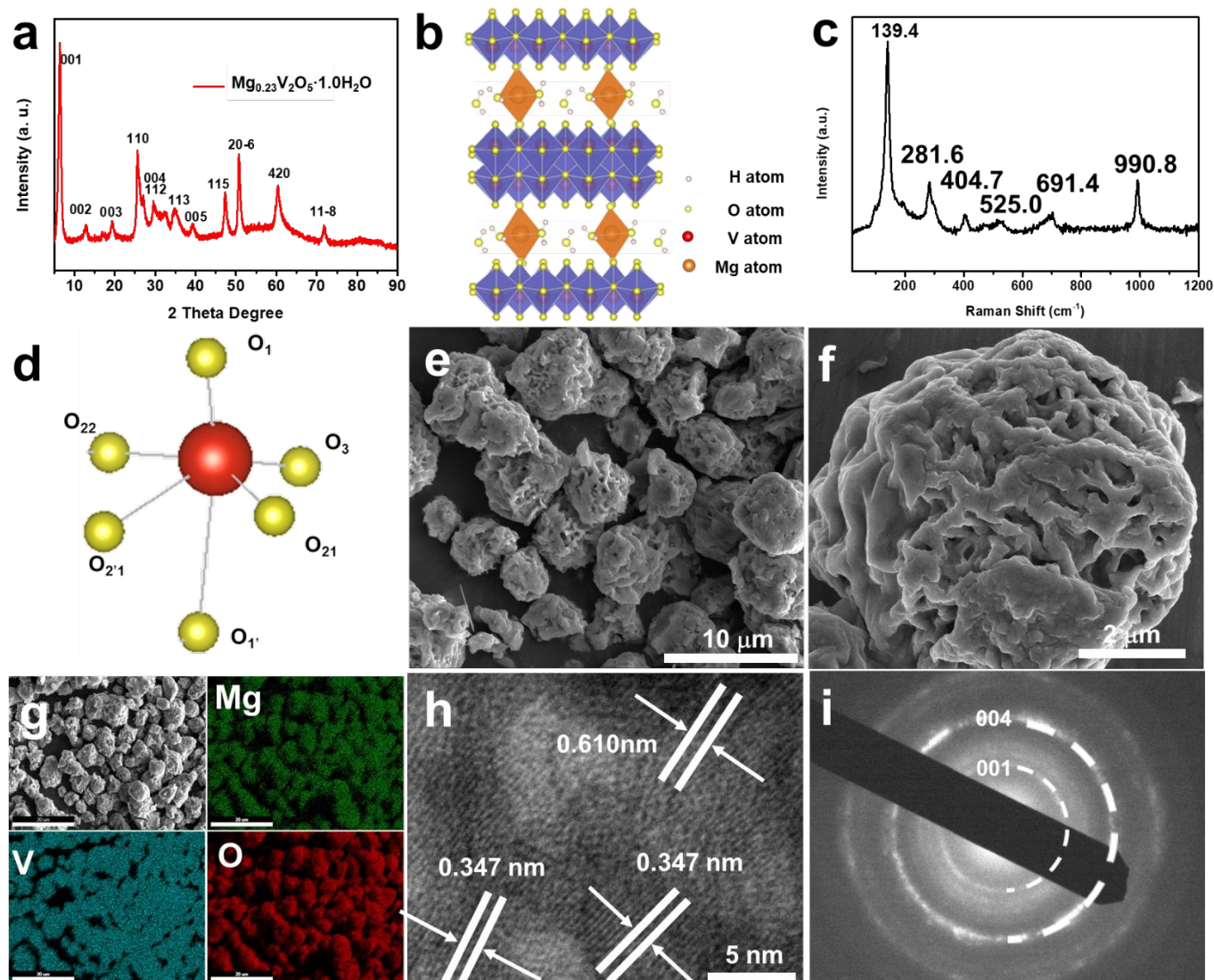


Figure 2. Structural characterization of MVO microspheres. (a) XRD pattern, (b) crystal structure, (c) Raman spectrum, (d) vanadium environments in MVO crystals, (e-f) SEM, (g) EDS elemental mapping, (h) HRTEM images and (i) SAED pattern

$\text{Mg}_{0.23}\text{V}_2\text{O}_5 \cdot 1.0\text{H}_2\text{O}$. The FTIR spectra (Fig. S9) confirms the structure of $\text{Mg}_{0.23}\text{V}_2\text{O}_5 \cdot 1.0\text{H}_2\text{O}$ microspheres. The peaks shown at 674, 924, and 451 cm^{-1} are attributed to $\nu_{\text{as}}(\text{V}-\text{O}_1-\text{V})$, $\nu_{\text{as}}(\text{V}-\text{O}_2-\text{V})$, and $\nu_{\text{s}}(\text{V}-\text{O}_1-\text{V})$ modes respectively. And the peak at high wavenumber of 1006 cm^{-1} is owing to the $\nu_{\text{s}}(\text{V}=\text{O})$ band. The large broad peak appeared at 742 cm^{-1} is assigned to symmetric stretching mode of $\nu_{\text{as}}(\text{V}-\text{O}_2-\text{V})$. The feature of FTIR result shown in Fig. S9 implies the layered structure of MVO. Specifically, the interlayer spacing can accommodate more H atoms bonding with O atoms due to the H-bonding effects, leading

to the decreased intensity of $\text{V}=\text{O}$ bond and intensified $\text{V}-\text{O}_1-\text{V}$ bond. FESEM and TEM were performed to study the morphological structure of MVO. As seen in Fig. 2e-f, MVO shows uniform microsphere morphology with porous and rough surface. The average diameter of microspheres is 7.4 μm . Moreover, as the magnified SEM images shown in Fig. 2f, numerous pores are present on the surface of MVO microspheres. The porous structure is beneficial for the electrolyte penetration and charge carrier diffusion. In comparison, the synthesized $\text{V}_2\text{O}_5 \cdot n\text{H}_2\text{O}$ possesses

ARTICLE

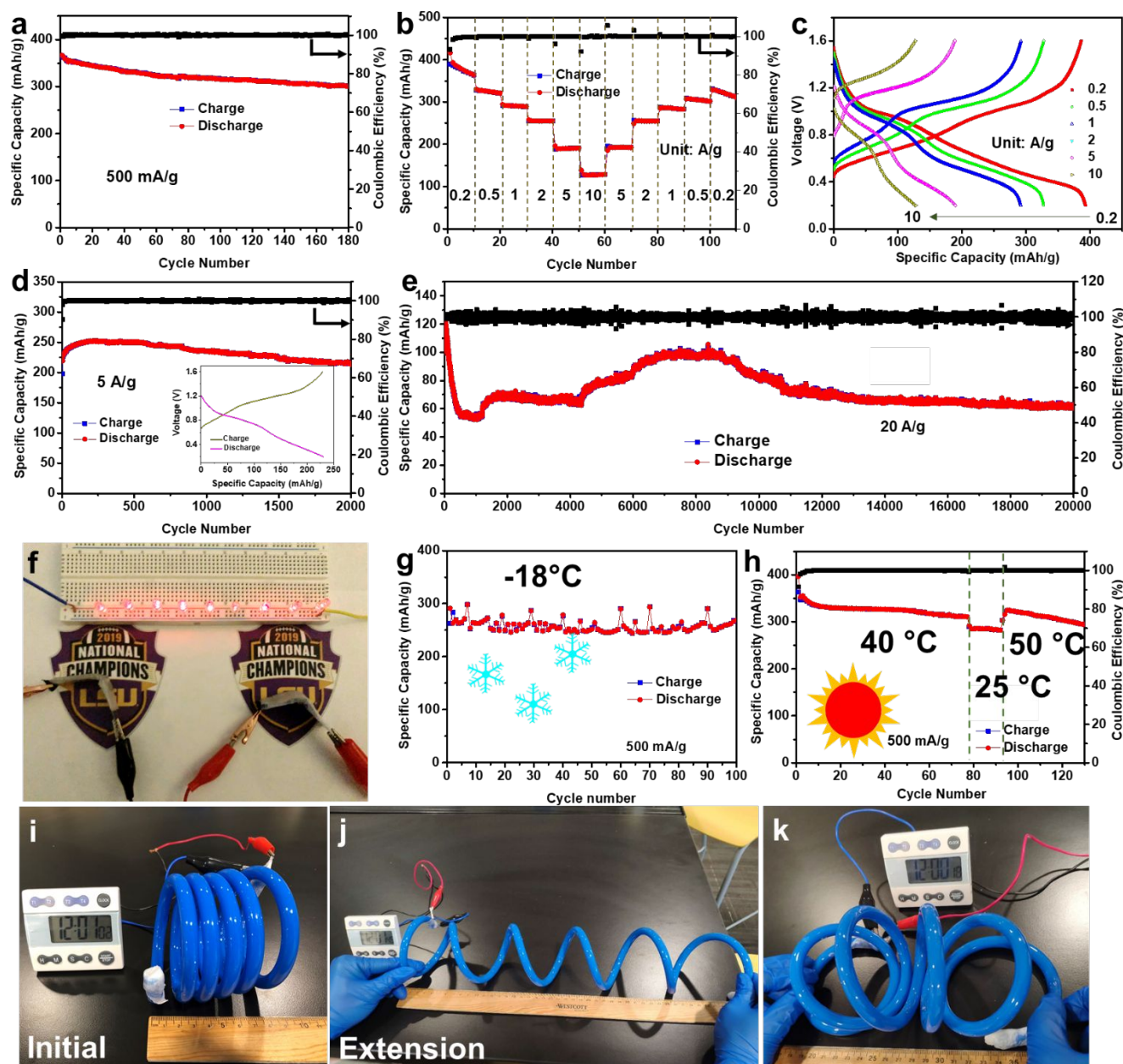


Figure 3. Electrochemical performance of MVO/Zn ssBs. (a) cycling performance at current density of 500 mA/g, (b) rate performance and (c) related charge/discharge profiles. Long cycling performance at the high current densities of (d) 5, (e) 20 A/g. (f) An optical photo of nine LED lights powered by two MVO/Zn ssBs with bending degree of 90°. Cycling performance at the current density of 500 mA/g with temperature condition of (g) -18 °C, (h) 40 °C and 50 °C. (i-k) the optical photos of a designed spring battery powered a watch.

nanowires morphology (Fig. S10). EDS mapping of MVO microspheres was performed to confirm the elemental composition. As shown in Fig. 2g, the magnesium, vanadium and oxygen signals were overlapped uniformly across the entire sample, which is

indicative of uniform compositions of MVO. From the XPS survey, the characteristic peaks of all elements (Mg, V, O) are displayed (Fig. S11). The atomic ratio of Mg/V calculated from the peak area is close to 23:200, which agrees with to the result of EDS mapping. In

addition, from the magnified XPS spectra of vanadium shown in Fig. S11c, the two peaks at binding energy of 516.2 and 517.7 eV can be assigned to vanadium at valance state of +4 and +5 respectively, further confirming the V_2O_5 framework was partially reduced with the preintercalation of Mg ions. As shown in Fig. S12, the 7.5 % weight loss suggests the stoichiometric formula of $Mg_{0.23}V_2O_5 \cdot 1.0H_2O$ for the obtained sample. The high-resolution TEM images display the crystallographic structure of MVO microspheres. The measured lattice fringes of 0.610 and 0.347 nm can be indexed as (003) and (005) planes. The SAED pattern shown in Fig. 2i confirms the polycrystalline nature of the as-prepared MVO microspheres.

3.3 Electrochemical Performance of ssZIBs

The ssZIBs were assembled using MVO as cathode, CNF-PAM film as electrolyte and separator, and zinc metal as anode. It should be noted that this process of assembling is facile and efficient and has potential for the industrial production. Fig. S13, S15 and 3a-h display the electrochemical performance of the as-assembled MVO/Zn solid-state batteries. Fig. S13 shows the CV curves of MVO microspheres in first three consecutive cycles. In the first cycle, two well defined reduction peaks are resolved at 0.92 and 0.50 V. Meanwhile, two corresponding anodic peaks located at 0.80 and 1.25 V can be observed as well. The cathodic peaks at 0.92 and 0.50 V are attributed to the intercalation of a certain amount of Zn ions into the interlayer space of MVO lattice and the related phase transformation. While the anodic peaks are ascribed to the oxidation of vanadium and return back into MVO with the extraction of zinc ions. In subsequent cycles, the peak position and peak shape of the third cycle are very close to that of the second cycle, showing high reversibility of Zn^{2+} ions insertion/extraction in MVO. Fig. 3a shows the cycling performance at the low current density of 500 mA/g. The MVO/Zn ssBs can deliver the high initial specific capacity of 367 mAh/g, which is comparable with the capacity of the aqueous MVO/Zn batteries.⁴⁵ While, the pure $V_2O_5 \cdot nH_2O$ can only deliver the reversible capacity of 281 mAh/g. (Fig. S14) After 180 cycles, the MVO/Zn ssBs still maintained the capacity of 300 mAh/g, with 81.7 % of the initial capacity retained, showing excellent capacity retention capability. In addition, from the rate performance illustrated in Fig. 3b, the MVO/Zn ssBs delivered the discharge capacity of 393, 330, 293, 257, 190, 130 mAh/g at the current density of 0.2, 0.5, 1, 2, 5, and 10 A/g, respectively. Moreover, when the current density recovered stepwise from 10 to 0.2 A/g, the capacity recovered to the previous value at each step of current, indicating excellent rate capability. The related galvanostatic charge-discharge plots during rate test are shown in Fig. 3c. The obvious plateaus are consistent with the CV results shown in Fig. S13. Then, the cycling stability was tested the at high current density of 5 and 10 A/g, respectively.⁴⁶ As illustrated in Fig. 3d and S13, after 2000 cycles, the batteries can still deliver the discharge capacity of 216 and 134 mAh/g, maintaining 98.6% and 75.3 % of the maximum value, showing high capacity and excellent capacity retention at high currents. To further test the ultralong-life cycling stability, we ran the batteries at the super-high current density of 20 A/g for over 20000 cycles. As displayed in Figure 3e, the maximum specific capacity was 119 mAh/g after 20000 cycles, the discharge capacity was maintained at 62 mAh/g (charging time of around 12 seconds), achieving about 52.1% capacity retention and almost 100%

Coulombic efficiency. The capacity loss at initial cycles is attributed to the sluggish diffusion of Zn^{2+} ions in gel electrolyte and within the electrode materials at super high current.^{47, 48} Moreover, current density is also the key parameter for the zinc anode performance. At super high current density, the intensity of electric field at zinc dendritic sites is much higher than that on the other areas. The dendritic growth during Zn electrodeposition leads to the capacity loss during cycles.⁴⁷ The comparison with other reported performance of ZIBs is listed in Table S1. It is worthy to note that the current MVO/Zn ssBs afford unprecedented long cycling life with the current density as high as 20 A/g for ssZIBs. Furthermore, we also evaluated the flexibility of MVO/Zn ssBs. As shown in Fig. 3f and the video shown in Supporting Information II, the MVO/Zn ssBs were still operational with the repeated bending from -180° to 180° , demonstrating excellent durability against mechanical deformation. To test the freeze-resistance capability of our MVO/Zn ssBs, the batteries were tested in a freezer at temperature of as low as $-18^\circ C$ with current density of 500 mA/g. As shown in Figure 3g, the batteries still maintained the specific capacity of 267 mAh/g for over 100 cycles without obvious capacity decaying, showing outstanding stability and anti-freezing capability. Moreover, under other conditions, such as cutting (Fig. S16), burning (Fig. S17) and high temperature of $40^\circ C$ and $50^\circ C$ (Fig. 3h), the MVO/Zn ssBs showed high stability and reliability.

The stretchability was also tested through stretching the developed spring ssZIBs. First, a spring solid-state battery was prepared by sealing the cathode, anode, and CNF-PAM hydrogel electrolyte in a spring-type plastic tube. As shown in Fig. 3i, the digital clock was powered by the developed blue spring solid-state battery. As the figure shown in Fig. 3j-k and the video shown in Supporting Information III and IV, the spring solid-state battery still worked well under repeated tension and contraction. This demonstrates the robust stability, high stretchability and flexibility of our ssZIBs.

3.4 Kinetics Analysis of Solid-state MVO/Zn Batteries

To intercalation behavior of zinc ions in MVO electrode is further investigated. As shown in Fig. 4a, with the increase of scan rate from 0.1 to 2.0 mV/s, the anodic peaks shift to higher potential and the cathodic peaks move to lower potential, which is ascribed to the increase of diffusion resistance with the increased scan rate. In principle, electrochemical kinetics can be analyzed *via* power-law formula as below:⁴⁹

$$i = av^b \quad (1)$$

wherw i is the current (A), a and b are variable parameters and v is the scan rate (V/s). In general, the b value represents the type of electrochemical charge storage reaction. If b value is closed to 0.5, the electrochemical reaction is dominated by diffusion-limited process; while if b equals 1, it is surface-controlled capacitive process. To calculate b value, $\log(i)$ is plotted versus $\log(v)$. As shown in Fig. 4b, the b value calculated from the slope of peak 1, 2, 3, 4 are 0.773, 0.823, 0.968 and 0.874, respectively, suggesting the capacity contributes from both diffusion and capacitive processes. Moreover, the power-law formula $i = av^b$ can be divided into two parts to quantify the capacitive (k_1v) and diffusion ($k_2v^{1/2}$) contributions:

$$i = k_1v + k_2v^{1/2} \quad (2)$$

or

$$i / v^{1/2} = k_1v^{1/2} + k_2 \quad (3)$$

where k_1 and k_2 represent the capacitive and diffusion contributions respectively. The calculated results of the contribution ratios at different scan rates are displayed in Fig. 4c. For example, at a scan rate of 0.2 mV/s, ~53.1% of the current is contributed by capacitive process, (Fig. S18) revealing that the electrochemical reactions of MVO are main affected by the capacitive process. With the increase of scan rate, the contribution of the capacitive contribution increases. To study the kinetics of MVO cathode, GITT is carried out and shown in Fig. 4d. The diffusion coefficient $D_{Zn^{2+}}$ (cm^2/s) can be determined based on the equation below:

$$D_{Zn^{2+}} = \frac{4l^2}{\pi t} \left(\frac{\Delta E_s}{\Delta E_t} \right)^2 \quad (4)$$

where l equals to the thickness of electrode, t is the time of applied current pulse, ΔE_s is the variation of steady-state potential for the related step, and ΔE_t is the potential change of a one-step GITT test after eliminating the iR drop. Fig. 4e displays the calculated Zn^{2+} diffusion coefficients of the MVO electrode at each step of GITT test. The average value of $D_{Zn^{2+}}$ for charging and discharging process is about $1 \times 10^{-7.32}$ and $1 \times 10^{-7.05}$ cm^2/s respectively, showing much higher value than that of $V_2O_5 \cdot 1.0H_2O$ electrode ($1 \times 10^{-7.74}$ and $1 \times 10^{-7.76}$ for charging and discharging respectively, Fig. S19) and the results published before.²⁴ The high Zn^{2+} diffusion coefficient value indicates fast charge-transfer kinetics. The EIS test was also carried out to investigate the interfacial charge transfer resistance. As shown in Fig. 4f, the MVO electrode displays the charge-transfer resistance as low as 127 Ω , much lower than that of $V_2O_5 \cdot 1.0H_2O$ electrode (313 Ω). The high diffusion coefficients and low resistance are attributed to the lattice water, which can shield the charge of intercalated Zn^{2+} , and also reduce the interaction between Zn^{2+} and host material, serving as "lubricant" to facilitate the diffusion process of Zn^{2+} ions.⁵⁰

3.5 Zinc-storage Mechanism in MVO Cathode

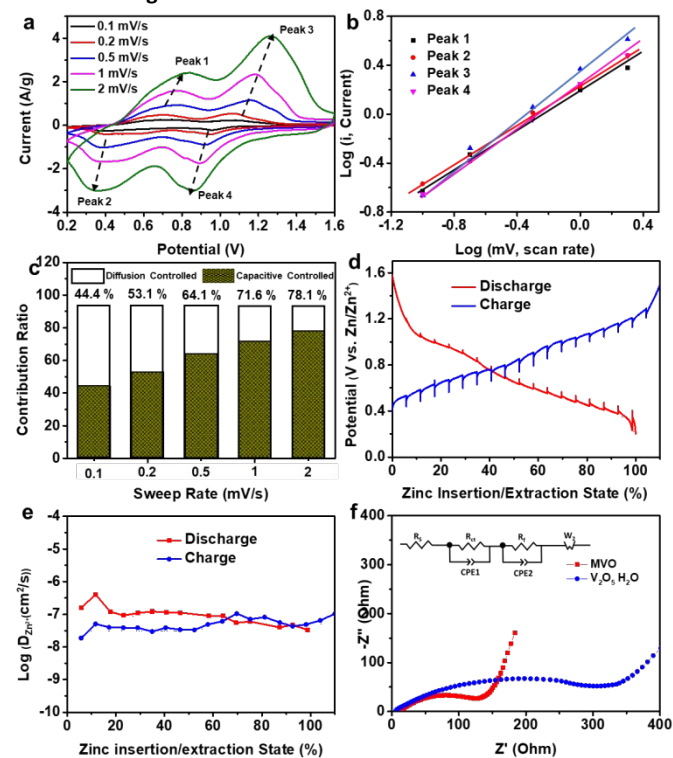


Figure 4. (a) CV curves at the scan rates of 0.1, 0.2, 0.5, 1, 2 mV/s, (b) Randles-Sevcik plot of cathodic and anodic peaks, (c) contribution ratio of the capacitive capacities and diffusion-limited capacities, (d)

GITT profiles of MVO electrode, (e) diffusion versus different Zn^{2+} insertion/extraction states, (f) Nyquist plots of MVO/Zn and V_2O_5/Zn batteries.

Fig. 5a-c display the XRD patterns of MVO at different charge/discharge states during the first two cycles. As shown in Fig. 5a, the intensity of characteristic (001) peak at 6.43° decreased dramatically during the initial discharge process, which is attributed to the structural change and the decrease of crystallinity with the intercalation of Zn^{2+} ions. Also, as observed in the magnified XRD patterns (Fig. 5c), the (001) peak shifts to higher angles after fully discharge. This is attributed to the contraction of the interlayer spacing. The formation of hydrogen bonds between inserted Zn^{2+} ions, structural oxygen and water pulled the layers closer. Moreover, from Fig. 5a and S19, obvious new peaks appeared at 33.1° and 69.2° , which can match well with $Zn_{0.29}V_2O_5$ (PDF#: 24-1480), suggesting that the new phase $Zn_{0.29}V_2O_5$ forms during the discharging process. This is probably attributed to the decrease of valance state of vanadium with the intercalation of zinc ions and ultimately the framework of monoclinic MVO is partially transformed into rhombohedral $Zn_{0.29}V_2O_5$. While, at the completely charge state, the new peaks disappear and the (001) peak returns to 6.66° , indicating high structural reversibility with the insertion/extraction of zinc ions. To further confirm the structure change, Raman spectra at different charge/discharge states are also measured. As shown in Fig. 5d, the intensity of dominate peak at 139.4 cm^{-1} decreases a lot with the voltage discharge to 0.2 V, suggesting the significant increase of the long-range disorder of the vanadium oxygen layers along the plane with the insertion of Zn^{2+} . Moreover, after the initial discharge to 0.2 V, the bands at 281.6 , 404.7 , 512.0 cm^{-1} shifts to lower frequency at 251.8 , 370.1 and 491.8 cm^{-1} , respectively. The shift in frequency of these bands is probably attributed to the lengthening of the $V-O_1$ and $V-O_2$ bonds for the $Zn_xMg_xV_2O_5$ phase. Notably, the band at 687.1 cm^{-1} completely vanishes; the band at 990.5 shifts to 865.2 cm^{-1} and strengthens significantly. These changes of vibration modes attribute to the change of MVO crystal structure upon the intercalation of zinc ions. The large interlayer spacing accommodates inserted Zn^{2+} ions and water molecules, which are bonded with lattice oxygen. Consequently, the formation of more H-bonding between H atoms and lattice oxygen leads to decrease the strength of $V=O$ and strengthen the $V-O-V$, resulting the shift of the bond vibration. The HRTEM images and SAED patterns in Fig. 5h-k further confirm that the phase transformation and structure change during charge/discharge. As shown in Fig. 5f, the measured lattice fringe of 0.274 nm can be indexed to the (104) plane of the appeared new phase $Zn_{0.29}V_2O_5$. As SAED pattern observed from Fig. 5g, it is obvious that the new phase disappeared, indicating that the structure change with the insertion/extraction of zinc ions are reversible. To further confirm the chemical state of MVO with the intercalation of zinc ions, XPS spectra were measured at different charge/discharge states. Fig. S22 and Fig. 5h-k display the XPS survey, high-resolution XPS spectra of V 2p, O 1s, Zn 2p and Mg 1s, respectively at the initial, fully discharge and charge states. The XPS survey in Fig. S22 and EDS mapping in Fig. S23 confirm the existence of Zn after the fully discharging. And as shown by the high-resolution XPS data (Fig. 5h), the V^{5+} signal at 516.4 eV largely increased upon the discharging state. This is attributed to the reduction of the valance value of V with the intercalation of zinc ions. At the fully charged state, the V^{5+} returns back to the dominate species, indicating reversible electrochemical redox reactions with

the insertion/extraction of zinc ions.^{51, 52} The reversible electrochemical reactions are also verified by the XPS spectra of the O 1s. As shown in Fig. 5i, at pristine and fully charged states, the O 1s

are fitted into three peaks at 530.3, 530.9, and 533.1 eV. While, at the fully discharge states, two broad new peaks appeared at 538.6

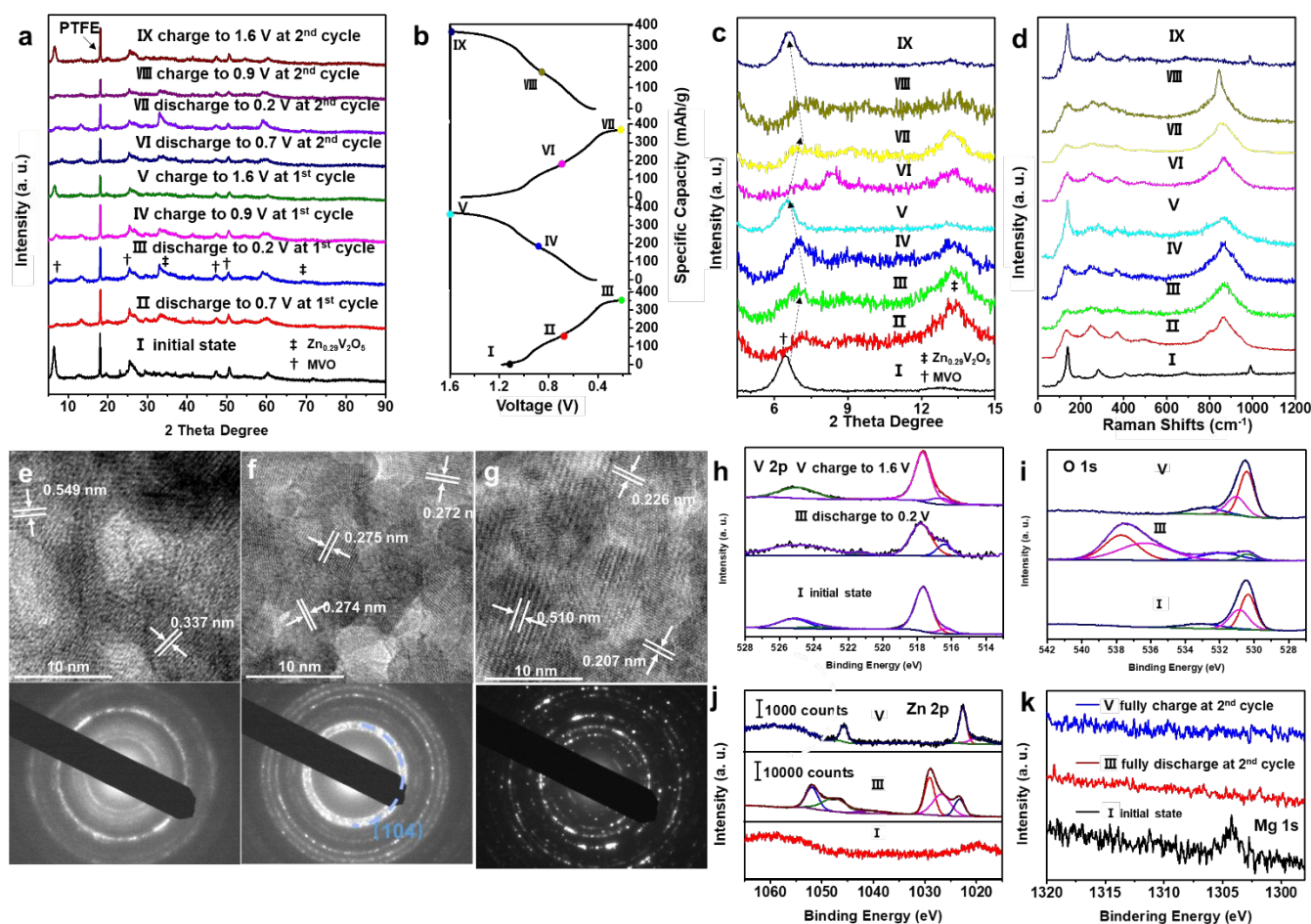


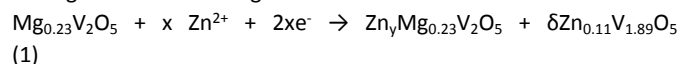
Figure 5. Ex situ structure and chemical state characterization of the $\text{Mg}_{0.23}\text{V}_2\text{O}_5 \cdot 1.0\text{H}_2\text{O}$ microspheres during the charge/discharge process. (a, c) XRD patterns and (d) Raman spectrum collected at different charge/discharge states, (b) the corresponding charge-discharge profiles in first two cycles; HRTEM images at (e) initial, (f) fully discharge, (g) fully charge states. XPS spectra of (h) V 2p, (i) O 1s and (j) Zn 2p (k) Mg 1s, at initial, fully discharge and charge states.

and 534.0 eV. The appeared two new peaks are ascribed to the inserted H_2O molecules and oxygen bonded with zinc ions in ZMVO.^{53, 54} In addition, the Zn 2p core level spectra provide a clear evidence for the reversible intercalation of Zn^{2+} ions during charging and discharging process. As shown in Fig. 5j, at the discharging state, two new pairs of Zn^{2+} peaks located at 1029/1052 and 1026/1047 eV are assigned to the bondings of the inserted Zn^{2+} ions in MVO. At the charging state, these new peaks disappeared, implying the extraction of Zn^{2+} in MVO. More importantly, it is obvious that the intensity of Zn 2p from insertion states is much higher than these at the extraction and initial states, suggesting the insertion/extraction of Zn^{2+} in/out of the MVO interlayer spacing. The Mg 1s region at different states is displayed in Fig. 5k. As shown in Fig. 5k, the signals of Mg are barely seen in the electrode material at discharge and charge states during the second cycle, indicating that most of the Mg^{2+} was deintercalated during the initial cycle. And the formed $\text{Zn}_x\text{V}_2\text{O}_5$ serves as the cathode material for the future cycles. Such phenomenon is known as the displacement/intercalation reaction mechanism, and it has also been

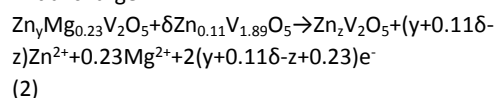
observed in $\text{Ag}_{0.4}\text{V}_2\text{O}_5$, $\text{Mg}_x\text{V}_2\text{O}_5 \cdot n\text{H}_2\text{O}$ and $\text{Na}_3\text{V}_2(\text{PO}_4)_3$ for ZIBs.^[55, 45, 56, 57]

Based on the results and discussion, we proposed the electrochemical reactions as shown in Fig. S24. The detailed reactions at each step are summarized as below.

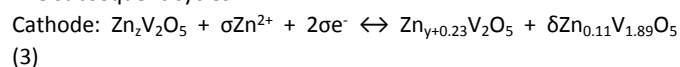
During the initial discharge on cathode:



Initial charge:



The subsequent cycles:



4. Conclusions

A superfast and stable ssZIB based on CNFs-PAM hydrogel electrolyte and $\text{Mg}_{0.23}\text{V}_2\text{O}_5 \cdot 1.0\text{H}_2\text{O}$ cathode was successfully developed from this work. The designed CNF-PAM hydrogel shows a high stretchability and robust mechanical stability. Moreover, the porous CNF-PAM hydrogel electrolyte provides efficient pathways for the transportation for zinc ions. And the robust layered structure of $\text{V}_2\text{O}_5 \cdot 1.0\text{H}_2\text{O}$ pillared with Mg^{2+} ions and water support the fast insertion/extraction of zinc ions in lattice. The prepared ssZIB shows remarkable high rate capability and long cycling performance. At the high current density of 5 A/g, the ssZIB provides a high specific capacity of about 216 mAh/g within charging time of only three minutes for over 2000 cycles, maintaining 98.6% of the initial capacity. Furthermore, with the designed CNF-PAM hydrogel electrolyte, the spring ssZIB was also obtained. The spring ssZIB is still workable under repeated stretching. Even under some critical states, such as repeated bending, freezing, and heating, the ssZIB shows high stability and reliability. The ssZIB shows extraordinary electrochemical performance, robust stability, high stretchability, which helps bring new opportunities for ZIBs for practical large-scale storage devices.

Conflicts of interest

There are no conflicts to declare.

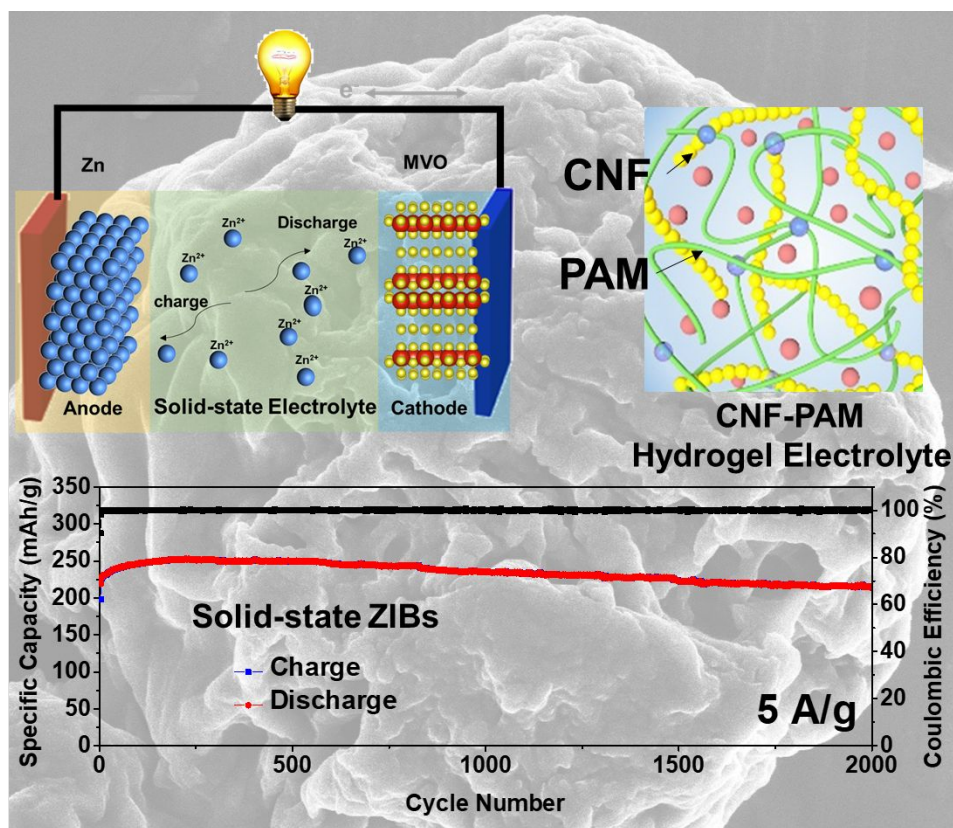
Acknowledgements

This work was financially supported by USDA Forest Service/US Endowment (Grant E17-23), Louisiana Board of Regents [LEQSF(2020-23)-RD-B-02; LEQSF(2018-19)-ENH-DE-06], National Institute of Forest Science (Seoul, Korea), and National Research Foundation of Korea (2018R1A2A1A05019733). We thank Dr. Kangning Zhao for his help on XRD Rietveld refinement analysis.

References

1. Y. Huang, H. Li, Z. Wang, M. Zhu, Z. Pei, Q. Xue, Y. Huang and C. Zhi, *Nano Energy*, 2016, **22**, 422-438.
2. Z. Liu, H. Li, M. Zhu, Y. Huang, Z. Tang, Z. Pei, Z. Wang, Z. Shi, J. Liu and Y. Huang, *Nano Energy*, 2018, **44**, 164-173.
3. S. Zhang, N. Yu, S. Zeng, S. Zhou, M. Chen, J. Di and Q. Li, *Journal of Materials Chemistry A*, 2018, **6**, 12237-12243.
4. X. Li, Y. Tang, H. Lv, W. Wang, F. Mo, G. Liang, C. Zhi and H. Li, *Nanoscale*, 2019, **11**, 17992-18008.
5. A. Manthiram, X. Yu and S. Wang, *Nature Reviews Materials*, 2017, **2**, 1-16.
6. S. Li, X. Meng, Q. Yi, J. A. Alonso, M. Fernández-Díaz, C. Sun and Z. L. Wang, *Nano Energy*, 2018, **52**, 510-516.
7. L. Mai, M. Yan and Y. Zhao, *Nature News*, 2017, **546**, 469.
8. X. Zuo, J. Zhu, P. Müller-Buschbaum and Y.-J. Cheng, *Nano Energy*, 2017, **31**, 113-143.
9. S. Li, D. Zhang, X. Meng, Q.-A. Huang, C. Sun and Z. L. Wang, *Energy Storage Materials*, 2018, **12**, 17-22.
10. K. Liu, Y. Liu, D. Lin, A. Pei and Y. Cui, *Science advances*, 2018, **4**, eaas9820.
11. L. Liu and C. Sun, *ChemElectroChem*, 2020, **7**, 707-715.
12. G. Zhou, F. Li and H.-M. Cheng, *Energy & Environmental Science*, 2014, **7**, 1307-1338.
13. X. Dong, L. Chen, X. Su, Y. Wang and Y. Xia, *Angewandte Chemie International Edition*, 2016, **55**, 7474-7477.
14. J.-Y. Luo, W.-J. Cui, P. He and Y.-Y. Xia, *Nature chemistry*, 2010, **2**, 760-765.
15. W. Xu and Y. Wang, *Nano-Micro Letters*, 2019, **11**, 90.
16. G. Fang, J. Zhou, A. Pan and S. Liang, *ACS Energy Letters*, 2018, **3**, 2480-2501.
17. J. Huang, Z. Guo, Y. Ma, D. Bin, Y. Wang and Y. Xia, *Small Methods*, 2019, **3**, 1800272.
18. T. Liu, X. Cheng, H. Yu, H. Zhu, N. Peng, R. Zheng, J. Zhang, M. Shui, Y. Cui and J. Shu, *Energy Storage Materials*, 2019, **18**, 68-91.
19. H. Pan, Y. Shao, P. Yan, Y. Cheng, K. S. Han, Z. Nie, C. Wang, J. Yang, X. Li and P. Bhattacharya, *Nature Energy*, 2016, **1**, 1-7.
20. Y. Zeng, X. Zhang, Y. Meng, M. Yu, J. Yi, Y. Wu, X. Lu and Y. Tong, *Advanced Materials*, 2017, **29**, 1700274.
21. H. Li, C. Han, Y. Huang, Y. Huang, M. Zhu, Z. Pei, Q. Xue, Z. Wang, Z. Liu and Z. Tang, *Energy & Environmental Science*, 2018, **11**, 941-951.
22. D. Wang, H. Li, Z. Liu, Z. Tang, G. Liang, F. Mo, Q. Yang, L. Ma and C. Zhi, *Small*, 2018, **14**, 1803978.
23. W. Liu, M. S. Song, B. Kong and Y. Cui, *Advanced materials*, 2017, **29**, 1603436.
24. J. Lai, H. Tang, X. Zhu and Y. Wang, *Journal of Materials Chemistry A*, 2019, **7**, 23140-23148.
25. Q. Yang, Y. Wang, X. Li, H. Li, Z. Wang, Z. Tang, L. Ma, F. Mo and C. Zhi, *Energy & Environmental Materials*, 2018, **1**, 183-195.
26. D. Chao, C. Zhu, M. Song, P. Liang, X. Zhang, N. H. Tiep, H. Zhao, J. Wang, R. Wang and H. Zhang, *Advanced Materials*, 2018, **30**, 1803181.
27. J. J. Xu, H. Ye and J. Huang, *Electrochemistry communications*, 2005, **7**, 1309-1317.

28. M. Li, J. Meng, Q. Li, M. Huang, X. Liu, K. A. Owusu, Z. Liu and L. Mai, *Advanced Functional Materials*, 2018, **28**, 1802016.
29. Z. Wang, J. Hu, L. Han, Z. Wang, H. Wang, Q. Zhao, J. Liu and F. Pan, *Nano Energy*, 2019, **56**, 92-99.
30. J. Zhang, M.-C. Li, X. Zhang, S. Ren, L. Dong, S. Lee, H. Cheng, T. Lei and Q. Wu, *Cellulose*, 2019, **26**, 4301-4312.
31. J. Zhang, Q. Wu, M.-C. Li, K. Song, X. Sun, S.-Y. Lee and T. Lei, *ACS Sustainable Chemistry & Engineering*, 2017, **5**, 7439-7447.
32. L. Ma, S. Chen, C. Long, X. Li, Y. Zhao, Z. Liu, Z. Huang, B. Dong, J. A. Zapien and C. Zhi, *Advanced Energy Materials*, 2019, **9**, 1902446.
33. X. Dai, F. Wan, L. Zhang, H. Cao and Z. Niu, *Energy Storage Materials*, 2019, **17**, 143-150.
34. P. Hu, T. Zhu, X. Wang, X. Wei, M. Yan, J. Li, W. Luo, W. Yang, W. Zhang and L. Zhou, *Nano letters*, 2018, **18**, 1758-1763.
35. J. Ding, Z. Du, L. Gu, B. Li, L. Wang, S. Wang, Y. Gong and S. Yang, *Advanced Materials*, 2018, **30**, 1800762.
36. Y. Yang, Y. Tang, G. Fang, L. Shan, J. Guo, W. Zhang, C. Wang, L. Wang, J. Zhou and S. Liang, *Energy & Environmental Science*, 2018, **11**, 3157-3162.
37. Y. Xu, X. Deng, Q. Li, G. Zhang, F. Xiong, S. Tan, Q. Wei, J. Lu, J. Li and Q. An, *Chem*, 2019, **5**, 1194-1209.
38. N. Zhang, F. Cheng, Y. Liu, Q. Zhao, K. Lei, C. Chen, X. Liu and J. Chen, *Journal of the American Chemical Society*, 2016, **138**, 12894-12901.
39. C. Xia, J. Guo, P. Li, X. Zhang and H. N. Alshareef, *Angewandte Chemie International Edition*, 2018, **57**, 3943-3948.
40. D. Kundu, B. D. Adams, V. Duffort, S. H. Vajargah and L. F. Nazar, *Nature Energy*, 2016, **1**, 16119.
41. C. Sanchez, J. Livage and G. Lucazeau, *Journal of Raman Spectroscopy*, 1982, **12**, 68-72.
42. D. Su and G. Wang, *ACS nano*, 2013, **7**, 11218-11226.
43. B. Yan, L. Liao, Y. You, X. Xu, Z. Zheng, Z. Shen, J. Ma, L. Tong and T. Yu, *Advanced materials*, 2009, **21**, 2436-2440.
44. A. Souza Filho, O. Ferreira, E. Santos, J. Mendes Filho and O. Alves, *Nano Letters*, 2004, **4**, 2099-2104.
45. F. Ming, H. Liang, Y. Lei, S. Kandambeth, M. Eddaoudi and H. N. Alshareef, *ACS Energy Letters*, 2018, **3**, 2602-2609.
46. B. Sambandam, V. Soundharrajan, S. Kim, M. H. Alfaruqi, J. Jo, S. Kim, V. Mathew, Y.-k. Sun and J. Kim, *Journal of Materials Chemistry A*, 2018, **6**, 15530-15539.
47. H. Kim, W. Choi, J. Yoon, J. H. Um, W. Lee, J. Kim, J. Cabana and W.-S. Yoon, *Chemical Reviews*, 2020.
48. Z. Cao, P. Zhuang, X. Zhang, M. Ye, J. Shen and P. M. Ajayan, *Advanced Energy Materials*, 2020, 2001599.
49. T. Brezesinski, J. Wang, S. H. Tolbert and B. Dunn, *Nature materials*, 2010, **9**, 146-151.
50. M. Yan, P. He, Y. Chen, S. Wang, Q. Wei, K. Zhao, X. Xu, Q. An, Y. Shuang and Y. Shao, *Advanced materials*, 2018, **30**, 1703725.
51. Y. Liu, Q. Li, K. Ma, G. Yang and C. Wang, *ACS nano*, 2019, **13**, 12081-12089.
52. T. Wei, Q. Li, G. Yang and C. Wang, *Advanced Energy Materials*, 2019, **9**, 1901480.
53. Q. Pang, C. Sun, Y. Yu, K. Zhao, Z. Zhang, P. M. Voyles, G. Chen, Y. Wei and X. Wang, *Advanced Energy Materials*, 2018, **8**, 1800144.
54. D. Kundu, B. D. Adams, V. Duffort, S. H. Vajargah and L. F. Nazar, *Nature Energy*, 2016, **1**, 1-8.
55. L. Shan, Y. Yang, W. Zhang, H. Chen, G. Fang, J. Zhou and S. Liang, *Energy Storage Materials*, 2019, **18**, 10-14.
56. G. Li, Z. Yang, Y. Jiang, C. Jin, W. Huang, X. Ding and Y. Huang, *Nano Energy*, 2016, **25**, 211-217.
57. S. Lian, C. Sun, W. Xu, W. Huo, Y. Luo, K. Zhao, G. Yao, W. Xu, Y. Zhang and Z. Li, *Nano Energy*, 2019, **62**, 79-84.



A solid-state zinc ion battery based on cellulose nanofiber-polyacrylamide hydrogel electrolyte and $\text{Mg}_{0.23}\text{V}_2\text{O}_5 \cdot 1.0\text{H}_2\text{O}$ cathode